Three-Dimensional Structure of Myosin Subfragment-1 from Electron Microscopy of Sectioned Crystals

Donald A. Winkelmann,* Timothy S. Baker,‡ and Ivan Rayment§

*Department of Pathology, Robert Wood Johnson Medical School, Piscataway, New Jersey 08854; ‡Department of Biological Sciences, Purdue University, West Lafayette, Indiana 47907; and §Department of Biochemistry and the Enzyme Institute, University of Wisconsin, Madison, Wisconsin 53705

Abstract. Image analysis of electron micrographs of thin-sectioned myosin subfragment-1 (S1) crystals has been used to determine the structure of the myosin head at ~25-Å resolution. Previous work established that the unit cell of type I crystals of myosin S1 contains eight molecules arranged with orthorhombic space group symmetry $P2_12_12_1$ and provided preliminary information on the size and shape of the myosin head (Winkelmann, D. A., H. Mekeel, and I. Rayment. 1985. *J. Mol. Biol.* 181:487–501). We have applied a systematic method of data collection by electron microscopy to reconstruct the three-dimensional (3D) structure of the S1 crystal lattice. Electron micrographs of thin sections were recorded at angles of up to 50° by tilting the sections about the two orthogonal unit cell axes in sections cut perpendicular to the three major crystallographic axes. The data from six separate tilt series were merged to form a complete data set for 3D reconstruction. This approach has yielded an electron density map of the unit cell of the S1 crystals of sufficient detail to delineate the molecular envelope of the myosin head. Myosin S1 has a tadpole-shaped molecular envelope that is very similar in appearance to the pear-shaped myosin heads observed by electron microscopy of rotary-shadowed and negatively stained myosin. The molecule is divided into essentially three morphological domains: a large domain on one end of the molecule corresponding to ~60% of the total molecular volume, a smaller central domain of ~30% of the volume that is separated from the larger domain by a cleft on one side of the molecule, and the smallest domain corresponding to a thin tail-like region containing ~10% of the volume. This molecular organization supports models of force generation by myosin which invoke conformational mobility at interdomain junctions within the head.

THE primary role of the interaction of actin and myosin is the generation of force and motion. This occurs as a consequence of the cyclic interaction of the motor domain of myosin with actin filaments and is driven by myosin ATP hydrolysis. Muscle myosin is a large, asymmetric, multi-domain molecule composed of six polypeptides: two heavy chains of molecular mass 220,000 D and two pairs of light chains of molecular masses 17,000–23,000 D (Warrick and Spudich, 1987). The carboxy-terminal portion of the myosin heavy chains associate to form an α-helical coiled-coil rod. The amino-terminal portion of each heavy chain associates with two different light chain to form an elongated globular domain; this structure contains the sites for hydrolysis of ATP and for binding actin (Margossian and Lowey, 1973). Myosin can be fragmented by limited proteolysis with papain, trypsin, and chymotrypsin into several structural and functional domains (Lowey et al., 1969; Weeds and Taylor, 1975). Major fragments that retain enzymatic or assembly properties have been prepared by cleavage in the rod to form heavy meromyosin (HMM)[1] and light meromyosin (LMM) or at the head–rod junction to form subfragment-1 (S1) and rod. These studies have led to the conclusion that it is the rod-like myosin tails that constitute the thick filament backbone, whereas the globular myosin heads (S1) lie on the surface of the filament. Furthermore, it has been demonstrated with an in vitro motility assay that the globular, actin binding head domain (S1) is sufficient to cause sliding movement of actin filaments (Toyoshima et al., 1987).

The complete sequence of genes coding for the myosin heavy chain and the myosin light chains have been determined for several invertebrate and vertebrate striated muscle and nonmuscle myosins (for review see Warrick and Spudich, 1987). This rapidly expanding sequence database has provided new insights into the structural and functional domains of the molecule. The deduced amino acid sequence of the myosin rod reveals a characteristic heptad repeat of charged and apolar residues with strong α-helical potential. However, aside from this characteristic repeat pattern, the homology between myosin rod sequences is not strong. In contrast, strong sequence homology exists among the deduced amino acid sequences of the S1 domains. Highly conserved regions of homology are found around a sequence believed to form part of the ATP binding site (Walker et al., 1982), around

1. *Abbreviations used in this paper*: HMM, heavy meromyosin; LMM, light meromyosin; S1, myosin subfragment-1; SF, structure factor; 3D, three-dimensional.

sites believed to be involved with actin binding and around two reactive cysteines (SH_1 and SH_2). Indeed, the sequence homologies within the S1 domain extend to a second class of myosin-like motor molecules referred to as myosin-I (Pollard et al., 1991). Myosin-Is differ from conventional myosin in that the long α-helical myosin rod domain is replaced by shorter, nonhelical sequences believed to have specialized binding functions. Lacking the coiled-coil rod domain necessary for dimerization, myosin-I exists as globular monomeric motors. Detailed analysis of myosin-I gene sequences reveals that the NH_2-terminal two-thirds of the deduced amino acid sequence covering the ATP and actin binding regions is homologous to the S1 domain of conventional myosin; thus these molecules represent a related but unique subclass of molecular motors. Unfortunately, the complete sequence of the S1 domain of myosin has yielded few insights into the secondary or tertiary structure of the myosin head.

Electron microscopy of myosin contrasted by rotary shadowing or negative staining has provided a progressively more detailed picture of the myosin heads. The heads appear pear-shaped and ~190–200 Å long, are thicker at the distal end and taper to the head-rod junction (Elliott and Offer, 1978). In negative stain the heads often appear curved and are subdivided by stain-filled clefts into a large domain at one end and two smaller domains near the junction of the head with the rod (Knight and Trinick, 1984; Walker and Trinick, 1988). The myosin light chains play an important role in determining the appearance and in stabilizing the structure of the myosin heads (Flicker et al., 1983; Walker and Trinick, 1989). Antibodies for both classes of light chain localize these subunits in the narrow region of the head near the junction with the rod (Flicker et al., 1983; Winkelmann and Lowey, 1986; Tokunaga et al., 1987*b*; Katoh and Lowey, 1989).

The organization of the heavy chain in the head has been studied extensively by proteolytic digestion of S1 (Balint et al., 1978; Mornet et al., 1981*b*; Applegate and Reisler, 1983). Limited tryptic cleavage of skeletal myosin S1 yields three major fragments of apparent molecular masses 25, 50, and 20 kD that are aligned in that order from the NH_2 terminus of the primary structure. These fragments remain associated under nondenaturing conditions and the cleaved head retains functional activity. A concept of "domains" that are linked by proteolytically sensitive regions has arisen from the finding that a variety of proteases cleave within 1–2 kD of the trypsin-sensitive sites (Applegate and Reisler, 1983; for review see Vibert and Cohen, 1988).

Detailed knowledge of the structure of the motor domain of myosin is essential for understanding the mechanism of all myosin based motility including muscle contraction. The discovery of conditions for crystallizing the head of myosin has lead to systematic studies of the S1 structure (Rayment and Winkelmann, 1984). Crystals of myosin S1 from avian skeletal muscle have been examined by x-ray diffraction and electron microscopy to determine how the molecules pack in the unit cell and to gain preliminary information on the size and shape of S1 in projection (Winkelmann et al., 1985). The appearance of the S1 in the crystal lattice is strikingly similar to the appearance of the heads on negatively stained or rotary shadowed myosin. However, these two-dimensional projections only provide limited information about the 3D shape and domain structure in the head. We present here the results of the application of a systematic method of data collection by electron microscopy used to record a complete data set for 3D reconstruction of the myosin S1 crystal lattice. This approach has yielded an electron density map of the unit cell of the S1 crystals of sufficient detail to delineate the molecular envelope of the myosin head at 25-Å resolution.

Materials and Methods

(a) Crystal Section Preparation

Myosin S1 crystals are formed with myosin isolated from chicken pectoralis muscle and cleaved with papain (Rayment and Winkelmann, 1984). This S1 preparation has both classes of myosin light chains (17 and 19 kD) and a 95-kD heavy chain for a total molecular mass of 130 kD. Purified preparations of chicken pectoralis muscle myosin S1 crystallize as thick, diamond-shaped, birefringent plates as previously described (Rayment and Winkelmann, 1984). The crystals belong to the orthorhombic space group $P2_12_12_1$ with unit cell dimensions a = 107 Å, b = 117 Å, and c = 278 Å. Crystals were fixed, prestained, dehydrated, and embedded as described (Winkelmann et al., 1985). Thin sections (300–500 Å thick) from crystals oriented with one of the three principal unit cell axes perpendicular to the cutting direction were picked up on Formvar coated grids, stained with uranyl acetate and lead citrate, and stabilized with a thin layer (<50 Å) of evaporated carbon.

(b) Electron Microscopy

Sections cut perpendicular to each of the three principal crystal axes were tilted from −45° to +45° in the electron microscope (Philips EM 420) in 3° or 6° steps and photographed at a magnification of 30,000× using low-irradiation methods to limit the total electron dose to ~120e^-/Å^2 (Baker and Amos, 1978). Objective lens was underfocused 3,000 Å such that, to the limit of resolution, all of the data were within the first zero of the phase-contrast transfer function (Erickson and Klug, 1971). Before photography, each section was oriented with a rotation specimen holder to align one of the two principal cell axes in the plane of the section along the microscope tilt axis. The orientation of the section was quickly aligned at low magnification (<1,000×) with the irradiation level limited to <0.02e^-/Å^2/s, and with the external crystal morphology used as a guide. At higher magnification (30,000×) the alignment was critically adjusted by rotating the untilted section to align a prominent set of striations along the direction of the tilt axis (coincident with one of the specimen translation controls). Each tilt series was obtained from a previously unirradiated area of the thin section, and the specimen area was refocused after each tilt increment.

(c) Image Analysis

Micrographs were surveyed by optical diffraction to assess the imaging conditions (defocus, astigmatism, specimen drift, and tilt) and to identify the best-preserved specimen areas (Salmon and DeRosier, 1981). Based on these criteria, we selected six tilt series (18 micrographs in each) recorded from four separate sections for processing using Fourier reconstruction methods (Baker, 1981; Amos et al., 1982). Selected tilt series include: series 02, which comprises 6° tilt increments over a range of +40° to −49° tilting about the b axis sampling the 0kl diffraction zone and designated 0kl(02), series 17 and 18 from adjacent areas of the same section comprising 3° tilt increments from −43° to 0° (series 17) and 0° to +52° (series 18) tilting about the c axis also sampling the 0kl zone and designated 0kl(17/18), series 07, which comprises 6° tilt increments from +47° to −43° tilting about the c axis sampling the h01 zone and designated h01(07), and series 25 and 26 from adjacent areas of the same section comprising 3° tilt increments from +50° to 0° (series 25) and −43° to 0° (series 26) tilting about the a axis and designated h01(25/26). Regions that gave sharp and strong diffraction spots for the entire set of 18 micrographs composing a single tilt series were selected and digitized on a 512 × 512 pixel array with an Optronics P1000 photoscan rotating drum microdensitometer (Optronics International, Chelmsford, MA) at a 25-μm raster step, which corresponds to 7.7 Å sampling of the original image. Care was taken to center the scanned array on precisely the same crystal area throughout the series of micrographs belonging to a tilt series. The last micrograph collected for each tilt series was a second untilted (0°) view to assess radiation damage.

Table I. Image Data Summary

Data set	No. of Films	Tilt step	Tilt range start	Tilt range end	Lattice spacing a	Lattice spacing b	Lattice spacing c	Phase residual*	Section thickness‡	z repeat
						Å				
0kl(02)	17	6°	−48.5°	+39.5°	z	118	276	18° ± 6°	330 Å	105 Å
0kl(17)	17	3°	−43.0°	0.0°	z	116	270	–	–	–
0kl(18)	17	3°	0.0°	+52.0°	z	117	268	17° ± 8°	300 Å	82 Å
h01(07)	17	6°	−42.5°	+47.0°	101	z	270	18° ± 6°	390 Å	112 Å
h01(25)	17	3°	+50.0°	0.0°	105	z	270	–	–	–
h01(26)	17	3°	0.0°	−43.0°	105	z	268	17° ± 5°	495 Å	104 Å

* Average and standard deviation of the amplitude weighted phase residual calculated as, $\Delta\alpha = \Sigma|\Delta\alpha(hkl)|\cdot F(hkl)/\Sigma F(hkl)$ and $-\pi \geqslant \Delta\alpha(hkl) \geqslant \pi$, on refining the films in a complete tilt series to a common phase origin.
‡ Section thickness and unit cell repeat normal to the section plane (z repeat) were determined from the projected maps of the reconstructed thin sections. Lattice dimensions on average are within 5% of values determined for hydrated crystals by x-ray diffraction.

These images were essentially identical to the first untilted images and were not processed.

The digitized images of specimen areas were displayed on a TV raster graphics device (Lexidata Corp., Billerica, MA), and then were boxed, floated and Fourier transformed (DeRosier and Moore, 1970; Baker et al., 1983). The computed diffraction patterns, representing separate central sections of the 3D Fourier transform of the finite crystal lattice, showed strong and sharp Bragg reflections at high tilt angles indicating excellent preservation of the 3D crystalline lattice in the thin section. Refined reciprocal lattice parameters were obtained for each diffraction pattern and structure factors (amplitudes and phases) were calculated from the computed Fourier transform out to 24 Å resolution (Baker and Amos, 1978; Baker et al., 1983). The position of the tilt axis and tilt angle, calculated from the observed, systematic changes of the lattice parameters in tilted views relative to the untilted view (Shaw and Hills, 1981), were used to locate each structure factor measurement along the lattice lines of the 3D Fourier transform of the thin section. The structure factor measurements were scaled to minimize differences between consecutive images of a data set and the origin position was iteratively refined to minimize phase differences between reflections within a z^* interval of 0.002 $Å^{-1}$ (Table I) (Amos et al., 1982). The discrete sampling of the combined phases and amplitudes of F(*hkz**) were fit to a smooth, evenly sampled function using a nonlinear least-squares fit of the observations to the transform of a constrained function of finitie extent by the method of Agard (1983) with the program LATLINE kindly provided by the author.

The interpolated structure factors for a tilt series were sampled at a z^* spacing of 0.0005 $Å^{-1}$ and were inverse Fourier transformed to reconstruct a density map for the thin section. The number of unit cells in the direction normal to the section plane was directly determined by projecting the map along one of the two cell axes in the plane (Table II). The reconstructed maps were averaged in the direction normal to the section plane over an integral number of unit cells to suppresses aliasing artifacts (DeRosier and Moore, 1970) and then Fourier transformed to produce a set of structure factors for the single unit cell.

(d) Data Merging

The process used to reconstruct the unit cell from a thin section and extract a unique set of structure factors for the unit cell was repeated for each of the tilt series data sets. Scaling and phase origin refinement, which was required to combine the independently processed data sets, was accomplished by comparing the structure factor measurements in common between individual data sets. Structure factors were scaled by equating $\Sigma|F(hkl)|$ for common structure factors between pairs of data sets. Data set 0kl(02) has the greatest overlap with data sets 0kl(17/18) (136 common SF's of 209 total) and h01(25/26) (131 common SFs of 203 total) and was therefore used as the reference for scaling these two data sets. Data set h0l(07) was then scaled to the combination of the three data sets.

Refinement of the independent data sets to a common phase origin utilized a reliability index, $R_{(A+B)}$, which measures the agreement of both the amplitude and phase of common structure factors between data sets, and is calculated as:

Table II. Statistics of Combined and Averaged Structure Factors

Data set	Total reflections	Unique reflections	Obs/total*	R‡	Δα(hkl)§ 1/40 Å⁻¹	Δα(hkl)§ 1/30 Å⁻¹	Δα(hkl)§ 1/25 Å⁻¹
			%				
0kl(02)	237	12	50	0.51	23	28	31
0kl(17/18)	209	64	44	0.25	6	9	11
h01(07)	235	67	50	0.47	22	28	30
h01(25/26)	203	3	43	0.48	27	39	41
(total)	(884)	(146)					
Combined	456/472		97	0.28	12	16	18

* Percentage of total reflections for calculation of the crystal structure to 25-Å resolution contributed by individual tilt series. Of the 472 possible reflections, 456 were measured in the combined data sets: 146 of these were measured once among the combined data sets, and 310 were measured between 2 and 4 times and averaged.
‡ The crystallographic R factor, calculated as $R = \Sigma||F(hkl)_o| - |F(hkl)_c||/\Sigma|F(hkl)_o|$; where $F(hkl)_c$ is the structure factor amplitude of the *hkl* reflection of the combined and symmetry averaged data set.
§ Amplitude weighted phase difference of structure factors calculated as
$\Delta\alpha = \Sigma|\Delta\alpha(hkl)\cdot F(hkl)_o|/\Sigma|F(hkl)_o|$ where, $\Delta\alpha = \alpha(hkl)_o - \alpha(\mathrm{hkl})_c$ $(-\pi \geqslant \Delta\alpha(hkl) \geqslant \pi)$, $\alpha(hkl)_o$ is the phase of the observed structure factor and $\alpha(hkl)_c$ is the phase of the combined and symmetry averaged structure factor. The magnitude of the phase difference and *R* factor indicate that the combined data are significant to the limit of resolution of the collected data, 25 Å.

$$R_{(A+B)} = \frac{\Sigma|F(hkl)_r - F(hkl)_o|}{\Sigma|F(hkl)_r|} \quad (1)$$

where $F(hkl)_r$ is the structure factor of the *hkl* reflection of the reference data set and $F(hkl)_o$ is the corresponding observed structure factor. The structure factor of a particular reflection may be represented by its amplitude ($F(hkl)$) and phase ($\alpha(hkl)$) or alternatively, by its real and imaginary parts, i.e., $F(hkl) = A + iB$, where $A = F(hkl)\cdot\cos\alpha(hkl)$, $B = F(hkl)\cdot\sin\alpha(hkl)$ and $|F(hkl)| = (A^2 + B^2)^{1/2}$. In this form, the reliability index used to bring two data sets to a common phase origin is written as:

$$R_{(A+B)} = \frac{\Sigma((A_r - A_o)^2 + (B_r - B_o)^2)^{1/2}}{\Sigma(A_r^2 + B_r^2)^{1/2}} \quad (2)$$

The magnitude of $R_{(A+B)}$ varies from values approaching 2.0 for unrelated data sets to values approaching the crystallographic R factor calculated as, $R = \Sigma||F(hkl)_o| - |F(hkl)_c||/\Sigma|F(hkl)_o|$, for data sets on a common phase origin with identical phases.

Data set 0kl(02) was chosen as the reference for refinement of h0l-(25/26). Refinement involved shifting the origin of the test file on a 3D grid, and sampling all possible combinations of Δx, Δy, and Δz. This pair of data sets was combined and h0l(07) was similarly refined to the origin of the combined pair. Finally, 0kl(17/18) was refined against the others. There was a clearly defined minimum in the search for a common origin with a 15% relative increase in the reliability index, $R_{(A+B)}$, between the lowest and the second lowest minima in the initial search between data sets 0kl(02) and h0l(25/26) and a similar difference on subsequent inclusion of the other data sets. The second best choice in each case was related to the best choice by one-half unit cell translation along one of the principal vectors. The individual data sets were combined and averaged, and the origin for the complete set of SFs was shifted to a position, midway between three nonintersecting twofold screw axes of the space group $P2_12_12_1$ and the SFs were averaged about the four symmetry-related positions of this space group. This combined and symmetry-averaged data set was used as the reference for another round of refinement with the individual data sets. At this stage the relative difference between the lowest and second lowest minima increases to 40–80%, essentially locking the choice of origin for each data set in place. This process was repeated two additional times until no further improvement was detected as measured by the reliability index, $R_{(A+B)}$. The combined and symmetry-averaged set of structure factors was used to calculate the 3D electron density map by Fourier summation using unit cell dimensions established by x-ray diffraction. The contour level used to define the boundary of the molecular envelope of myosin S1 was selected based on the assumption that 8 molecules of S1 (with molecular mass 130,000 D and partial specific volume 0.72 cm^3/g; Margossian et al., 1981) occupy ~36% of the volume of the 107 Å × 117 Å × 278 Å unit cell. Maps contoured at this volume clearly reveal the overall shape and contacts of the molecules in the unit cell.

(e) Model Building of Myosin and Actomyosin

Representations of two- and three-dimensional density distributions were displayed on the raster graphics device and photographed with a graphics recorder (ImageCorder 4566; Focus Graphics, Redwood City, CA). Three-dimensional contour maps were converted to polygonal element models then manipulated and displayed with the general purpose graphics display program, Movie.BYU (Department of Civil Engineering, Brigham Young University, Provo, UT). Models of acto-S1 were constructed based on the geometry of this complex as described by Milligan and Flicker (1987) and the 20-Å resolution model of F-actin as described by Egelman and DeRosier (1983). Actin is modeled as two intersecting spheres, each with radius 19 Å and a center-to-center separation of 30 Å. The position of the two spheres with respect to the helical filament axis are $\Delta z = 10$ Å, $\Delta\theta = 70°$, $r_1 = 11$ Å and $r_2 = 35$ Å, as defined by Egelman and DeRosier (1983). The helical parameters for the one-start left handed helix are −167° rotation per 27.8-Å rise per subunit that results in a crossover of the long pitch, two-start, right handed helix every 378 Å. Fourier transforms were calculated from two-dimensional projections of four repeats of modeled acto-S1 filaments, and layer-line data were extracted for comparison to published layer-line data for averaged filaments of acto-S1 (kindly provided by Ron Milligan, Scripps Institute, La Jolla, CA). A myosin rod segment was modeled by two 10-Å diameter rods entwined in a left-handed helix with a pitch of 162 Å/turn.

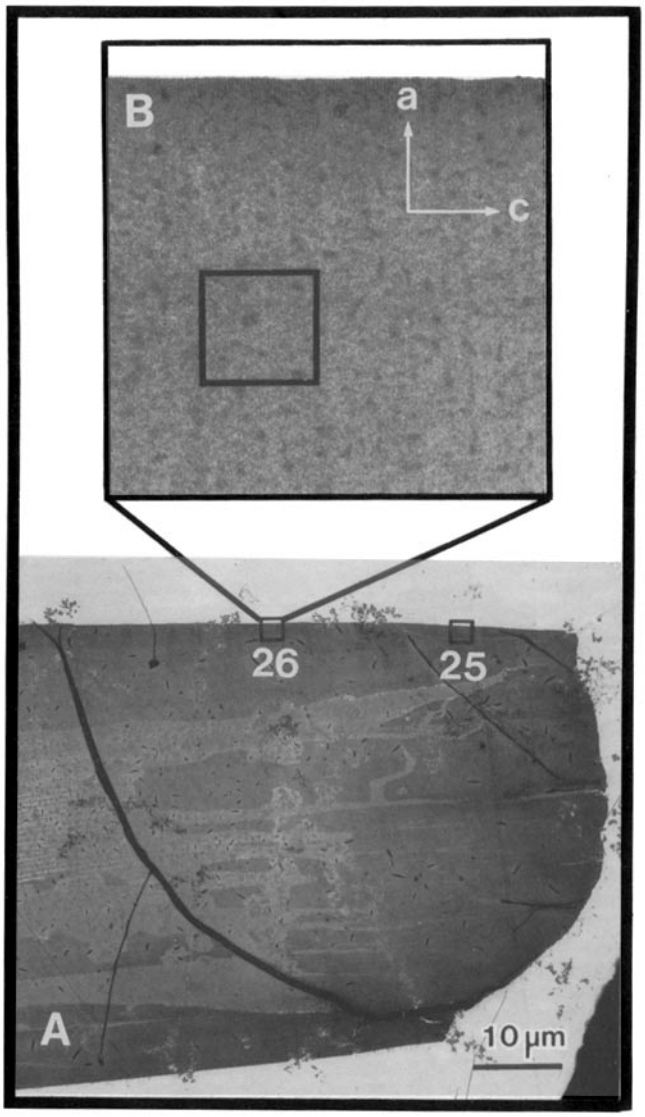

Figure 1. Thin section of myosin S1 crystal cut close to the [010] planes showing two areas from which tilt series images were recorded. (*A*) Low-magnification image (taken after data collection) that reveals the overall morphology of the 500-Å thick section that was cut perpendicular to the *b* axis of the crystal. The numbered boxes represent areas from which tilt series images were recorded. The edge of the sectioned crystal that was parallel to the *c* axis was used to align the *a* cell axis on the tilt axis of the microscope goniometer stage for tilt series 25 and 26. (*B*) Enlarged view of selected area of crystal section showing boxed region that was processed for tilt series h0l(26).

Results

Electron Microscopy and Image Analysis

Small, diamond-shaped crystals of myosin subfragment-1 were embedded with the tannic acid procedure of Akey et al. (1980). The morphology of these crystals made it possible to orient them physically during the embedding and sectioning procedure so that sections could be cut perpendicular to each of the major crystallographic axes (Winkelmann et al., 1985). This feature was exploited to collect systemati-

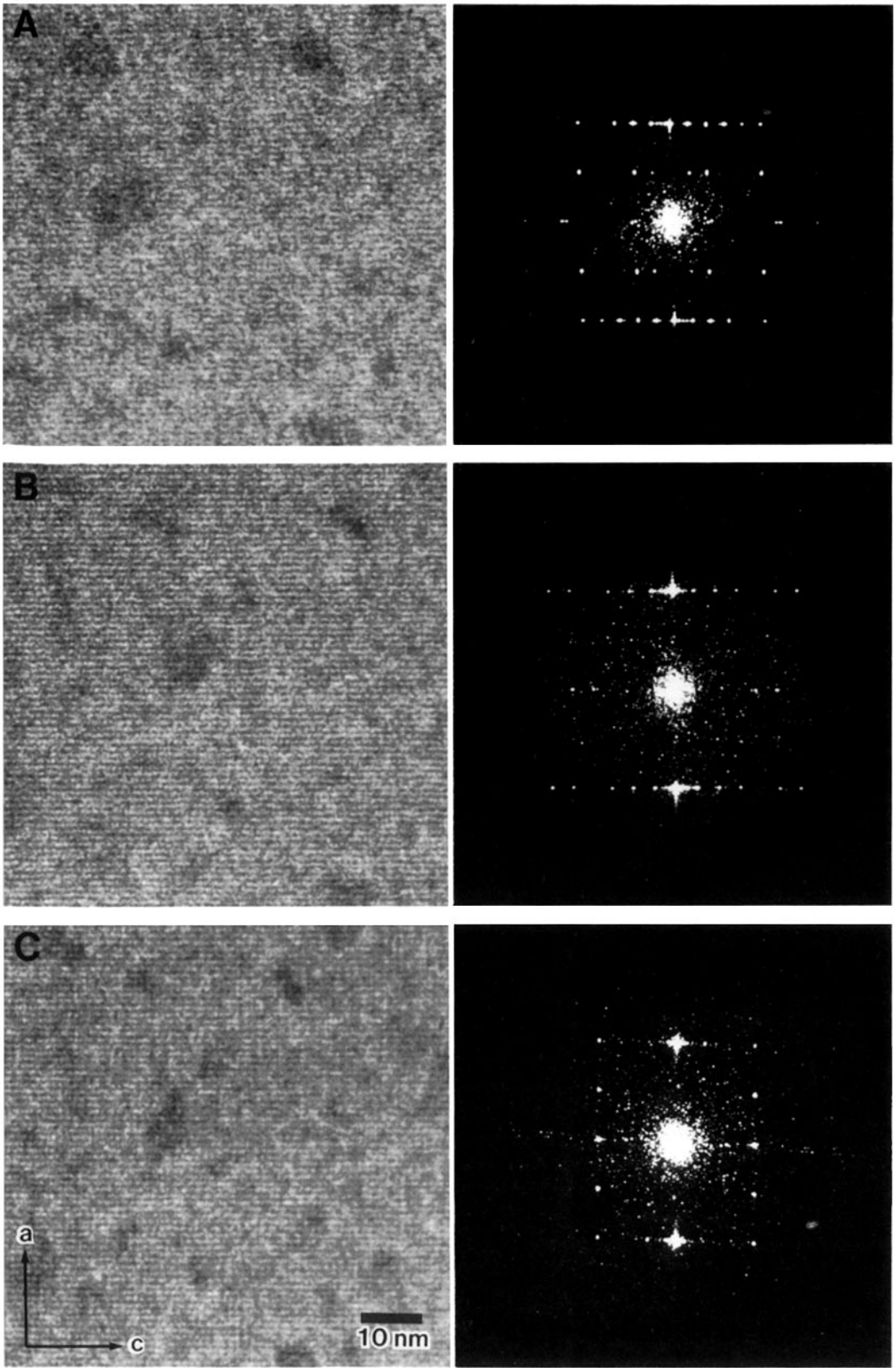

Figure 2. Scanned areas of section cut close to the [010] planes (*A*) 0° (untilted), and tilted (*B*) −31°, and (*C*) −46° about the *a* axis. Computed diffraction patterns from each image are shown alongside the corresponding image. The diffraction pattern of the untilted specimen (*A*) shows well-preserved mm symmetry and the absence of odd indexed reflections along both the *h* (*horizontal*) and *k* (*vertical*) reciprocal lattice axes. The occurrence of these systematic absences is consistent with plane group *pgg* symmetry, corresponding to the space group $P2_12_12_1$ in projection. The diffraction patterns change symmetrically (maintaining *mm* diffraction symmetry) as the specimen is tilted about *a* with reflections disappearing and reappearing and the spacing between reflections along c^* increasing, in a manner that is consistent with the sampling of a 3D crystalline lattice by tilting the specimen.

cally electron micrographs of oriented crystal sections tilted about the principal cell axes of the crystal. Data sets were collected for tilts about both axes of two orthogonal faces (the [100] and [010] planes), and these tilt series were independently reconstructed to produce a 3D density map of each crystal section. Due to limitation in the tilt range of conventional microscopes, each independent tilt series samples only a portion of the repeating structure of the crystal section, and the resulting maps contain artifacts resulting from this missing information typically observed as density features that become smeared in the direction perpendicular to the plane of the section (Agard and Stroud, 1982). However, the independent tilt series overlap each other to a varying extent and the combination of different views that were selected was sufficient to produce a final averaged density map of the repeating unit of the crystal that contained no missing information. This approach made it possible to collect a complete and oversampled data set to calculate the structure of the repeating unit in the crystal, and thereby minimize artifacts which result from missing data and provide a reconstructed density map with isotropic resolution.

Large areas of crystalline material were well preserved at the edge of crystal sections (Fig. 1). In contrast, central regions of crystals were poorly preserved, probably as a consequence of poor penetration of the fixatives. The inset shows a typical region selected for processing (Fig. 1 *b*). The edge of the crystal is very well defined as is the repeating pattern characteristic of this projection. The crystal was oriented in the block such that this section was cut perpendicular to the [010] planes (i.e., perpendicular to the *b* unit cell axis). In this orientation the *c* axis runs along the horizontal face of the crystal and the *a* axis is vertical. The section was oriented with a rotation holder to align the *a* axis close to the tilt axis of the microscope (see Materials and Methods). The appearance of the section when tilted by 0°, −31°, and −46° about the *a* axis, and the corresponding computed diffraction patterns reveal the excellent preservation of crystallographic symmetry in this section over the areas used for processing (Fig. 2). Since the horizontal striations from the *a* repeat are prominent in all images in this series, it's apparent that the tilt axis and the *a* unit cell axis are nearly parallel. The diffraction patterns calculated from the three regions shown reveal a systematic absence of reflections which is consistent with plane group *pgg* symmetry in the untilted section; variations in the diffraction patterns with tilt angle are also revealed (Fig. 2). The spacing between reflections varies systematically and individual reflections are seen to appear, disappear, and then new ones appear as the section is tilted; this is precisely the behavior expected for sampling of a 3D crystalline lattice (Berger, 1969).

3D Reconstruction

Each view of a tilted or untilted crystal section contributes a central plane to the 3D Fourier transform of the crystal section. The sampling of the 3D Fourier transform is limited by the number of images taken and is non-uniform. To calculate the 3D map of a crystal section a set of uniformly sampled amplitudes and phases for each structure factor must be derived from the observed amplitudes and phases. To obtain a uniformly sampled set of structure factors, the discretely sampled data from the computed Fourier transforms for each lattice point were fit to a line based on a $(\sin x)/x$ "sync" function that takes into account knowledge of the section thickness and uses a least-squares procedure for minimizing the error between the calculated and observed values of the amplitudes and phases (Agard, 1983).

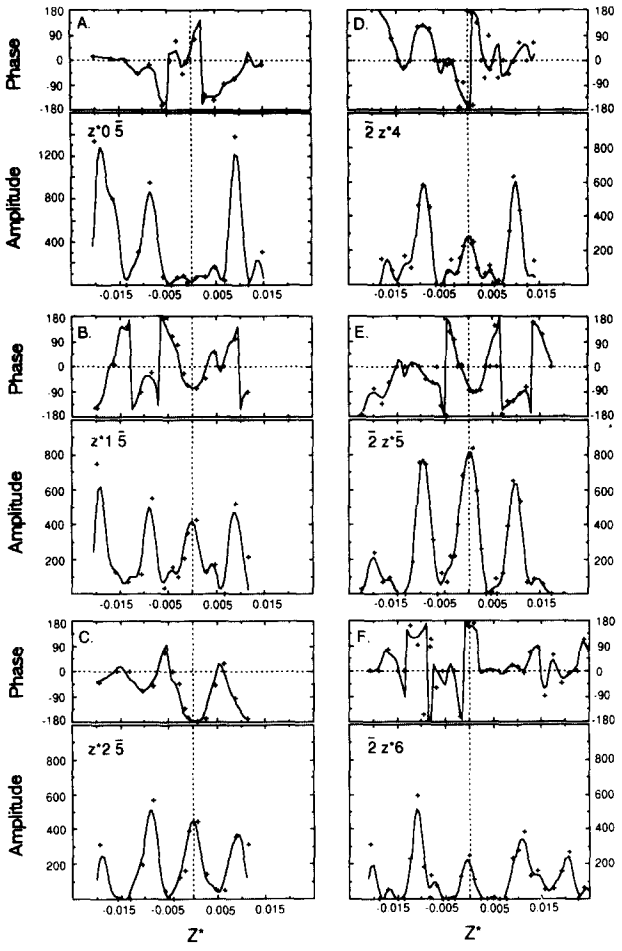

Figure 3. Plot of variation in the amplitudes and phases as a function of z^* (Å^{-1}) for three lattice lines from data set 0kl(02) (*A–C*), and three lattice lines from data set h0l(25/26) (*D–F*). The curves were obtained by a least-squares fitting procedure (Agard, 1983) and are not constrained by space group symmetry (plane group *pl* was assumed). The amplitudes show peaks at z^* spacings that correspond to values expected for the crystal unit cell reciprocal lattice spacings (Table I) indicating excellent preservation of the crystal lattice in the direction perpendicular to the plane of the thin section. The phases are relatively flat across the amplitude peaks and fluctuate between peaks. The smooth curves were sampled at a z^* spacing of 0.0005 Å^{-1} to derive the amplitudes and phases of the structure factors, F(*hkz**), used to reconstruct the 3D density distribution in each thin section examined.

Representative plots of the structure factor amplitudes and phases for six lattice lines, three from a tilt series about the a^* axis of the h0l zone (25/26) and three from a tilt series about the b^* axis of the 0kl zone (02), are shown in Fig. 3. Two-dimensional crystalline arrays give rise to a continuous Fourier transform in the direction perpendicular to the crystal plane (z^*). In contrast, these crystal thin sections yielded a distinctly sampled Fourier transform which shows up as several uniformly spaced peaks in the lattice line plots. The spacing of these peaks corresponds closely to the lattice dimensions of the hydrated crystals (Table I) and represent

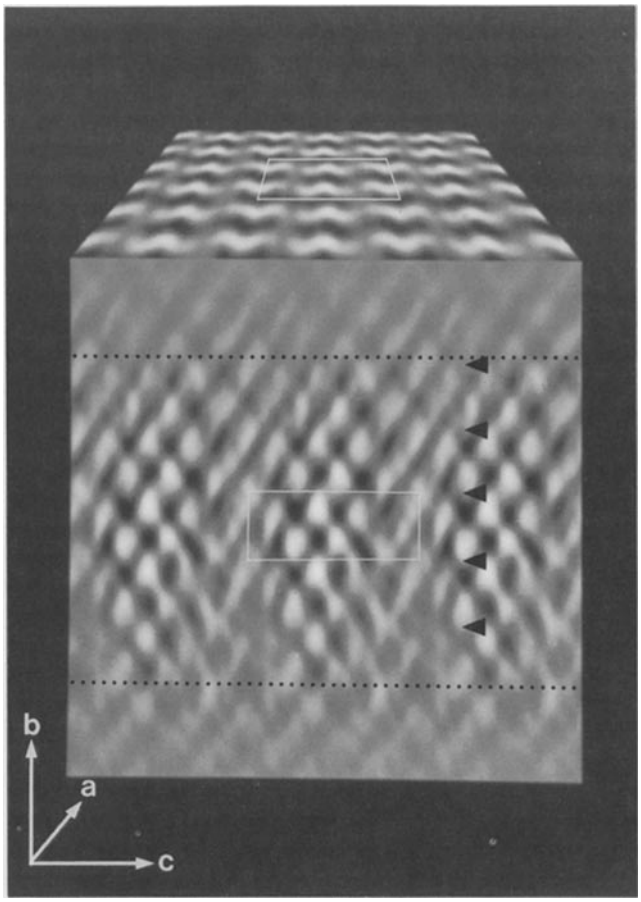

Figure 4. Two-dimensional projections of the 3D reconstruction of a thin section of an S1 crystal. Two distinct projections of the thin section are shown in perspective to provide a sense of how the data were collected and analyzed. Images from data set h0l(25/26) were collected from a thin section, which was tilted about the *a* axis. The view down *b* (shown in perspective) has the appearance that is characteristic of this projection of the crystal (Winkelmann et al., 1985), and one unit cell is outlined. The projected view down *a* is derived from reconstructing the thin section by Fourier summation of the structure factors, F(*hkz**), taken from the lattice line plots. This view of the thin section reveals at least four full repeats of the unit cell along *b* (marked by *arrows*). The dotted lines mark the approximate bounds of the thin section. The box in the center of the density map indicates one repeating unit. The smearing of density along *b* is a consequence of the "missing-wedge" of Fourier data. The alternating fuzzy and clear regions running along *c* arise from errors in the data and are apparent because the symmetry along *c* was not enforced in constructing this map. As a result, there is variation in the repeating units along *c*. The sources of error in the data include differences in amplitude scaling of the high tilt micrographs, variation in the range of sampling on either side of the tilt series, and drift in the phase origin on combining the data. The effects of these sources of error were minimized by averaging several individual unit cells extracted from the reconstruction of the section to produce a set of SFs representing the single average repeating unit. This averaging suppressed the "fuzzy-clear" pattern, whereas averaging combined with enforcing the symmetry eliminated it (data not shown).

the unit cell repeat of the crystal lattice in the z^* direction. This was a consistent property of all of the tilt series used in the reconstruction. It indicates that minimal shrinkage of lattice dimensions had occurred as a consequence of crystal embedding, sectioning, and electron microscopy and that each section contained multiple repeats of the crystal unit cell in the z^* direction.

The interpolated structure factors from the lattice line fitting procedure were used to generate a 3D reconstruction of each section by Fourier inversion. The section thickness and the number of repeating units in the direction normal to the section plane was directly determined by projecting the map along one of the cell axes in the plane (Fig. 4). Approximately 4 1/2 repeats are observed in the reconstruction of a section tilted about the *a* axis of the h0l zone. Features of the map are smeared in the *b* direction due to the absence of the "missing wedge" of Fourier data; nonetheless, the individual repeats are easily discerned. In order to combine data sets from different sections of varying thickness, the reconstructed maps were averaged in the direction normal to the section plane over an integral number of repeating units and the averaged map was Fourier transformed to yield a set of structure factors for a single, averaged unit cell representative of the crystal section. This approach was repeated for the tilt series from each of the sections included in the final reconstruction.

Structure factors from the separate reconstructed unit cells were then combined with an iterative scaling and phase origin refinement procedure, maximizing the fit among the data common to the individual data sets (Table II). The six tilt series from four individual crystal sections accounted for 96% of the structure factors required to compute a reconstruction at a resolution limit of 25 Å. Over two-thirds of the reflections were measured in two or more data sets. This redundancy provided a firm basis for determining a common phase origin to correctly combine the different data sets.

3D Map of S1 Crystal

The 3D map of the crystal unit cell calculated with the space group symmetry $P2_12_12_1$ imposed is essentially identical in the [100] projection (Fig. 5 *a*) to the two dimensional maps that have been published (Winkelmann et al., 1985). The three dimensional structure presented as a surface view, contoured at 83% of the volume of the protein in the crystal unit cell (Fig. 5, *b* and *c*), reveals the packing of the myosin heads. The elongated tadpole-shaped density features, which are interpreted as corresponding to single myosin heads, are arranged in essentially two layers (Fig. 5 *c*) perpendicular to *a*. There are strong head to tail contacts between molecules related by the 2_1 screw axes running parallel to *c*, and head to head contacts between molecules related within the plane by a local twofold rotation axis parallel to *a*. Strong contacts between the layers are found in only the thickest portion of the curved heads (Fig. 5 *c*).

Eight molecules of myosin S1 are packed in the unit cell with two molecules in the asymmetric unit. These two molecules, which can be seen stacked one on top of the other in Fig. 5 *c*, are not related by crystallographic symmetry operators in this space group and thus, are not averaged when the space group symmetry is imposed during calculation of the density map. Hence, small differences can be seen in the molecular envelope of these two molecules (Fig. 5 *c*). The regions which vary between the two molecules are the volume of the low density tail of the tadpole-shaped head and the depth of a cleft in the central region of the thick portion of the head. These variations are not interpreted as reflecting

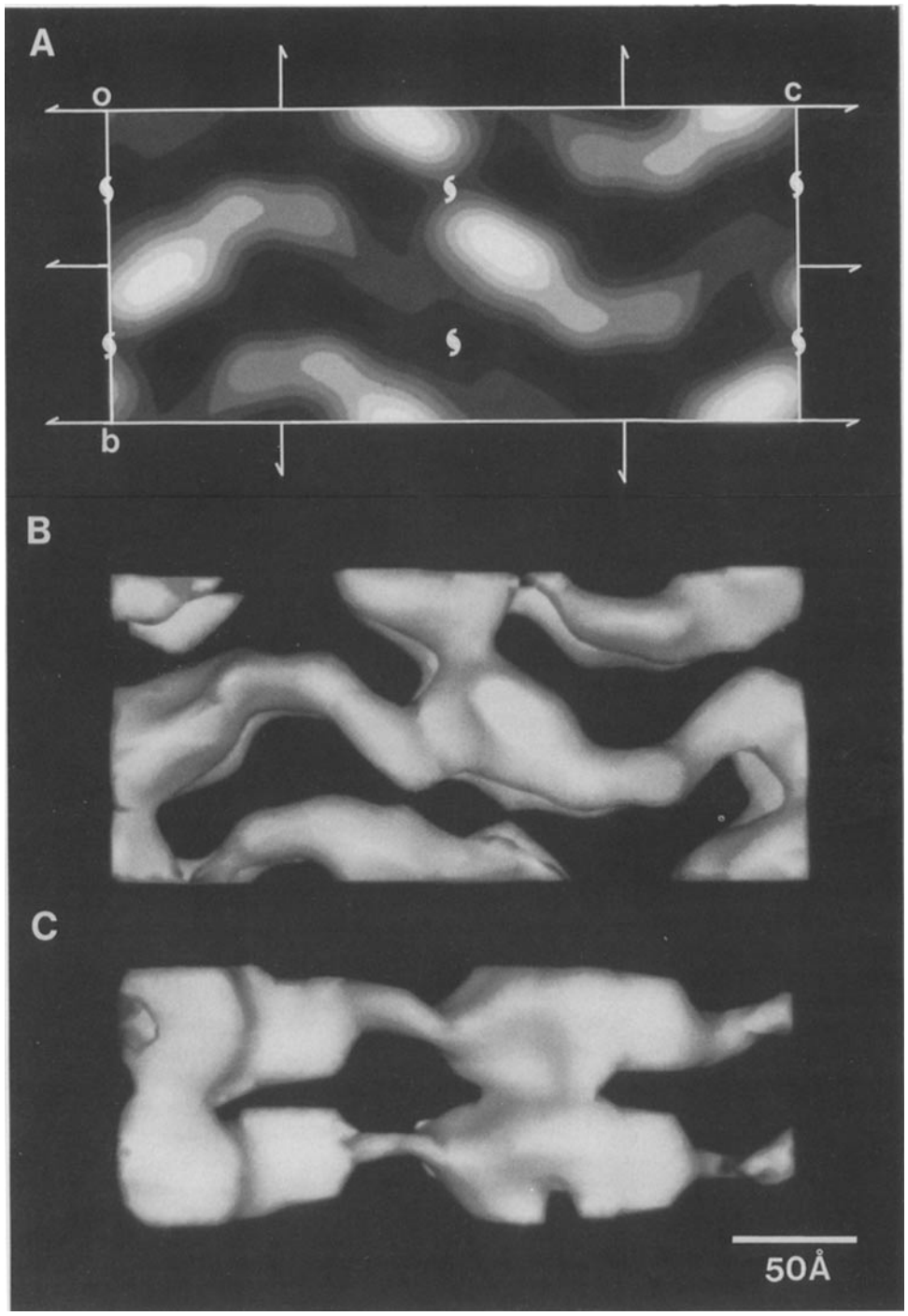

Figure 5. Two- and three-dimensional maps of the crystal unit cell calculated from the combined and symmetry averaged structure factors. (*A*) Contour display of the two-dimensional projection of a single unit cell of the final three-dimensional electron density map viewed down *a*. Orthorhombic space group symmetry $P2_12_12_1$ is imposed and the location of the projected symmetry operators corresponding to this space group are shown. (*B*) Surface-shaded representation of the 3D structure of the crystal unit cell view as in (*A*). The contour level used to define the surface of the stain excluding protein regions in the crystal was 83% of the hydrated molecular volume of myosin S1. At this contour level the limits of the elongated, tadpole-shaped S1 molecules are clearly resolved. (*C*) View down *b* of the unit cell (rotated counterclockwise 90° with respect to view in *B*) showing the arrangement of the heads in layers with strong contacts between the high density region of S1 molecules from different layers. For clarity, only the central pairs of symmetry related S1 molecules are shown in this view. The two S1 molecules in each layer are related by a 2_1 screw symmetry operator running along *c*, but S1 molecules stacked on top of one another are not related by crystallographic symmetry and thus are not averaged together. The small differences that exist between these two non-symmetry averaged molecules is likely to be representative of the noise level remaining in the averaged data.

different conformations of the two heads, since these two molecules are related by a local noncrystallographic symmetry operator (Winkelmann et al., 1985); the differences reflect the fact that these two molecules are not symmetry-averaged during calculation of the map and the magnitude of the differences is a measure of the residual noise in the data.

S1 Molecular Envelope and Domains

Despite the strong contacts between individual molecules within and between layers, the molecular envelope of a single head is readily delineated at this contour level when views down both the *a* and *b* axes are considered. In addition, the density map can be calculated with both the crystallographic and local symmetry imposed to average the two molecules in the asymmetric unit and produce a single average molecular envelope of myosin S1 (Fig. 6). The molecules are displayed with the surface contour level set to give ~83% of the hydrated volume of S1 (1.3×10^5 Å^3): at this volume, the length of the curved S1 is 165 Å with a longest cord of 145 Å. The molecule can be divided (Fig. 6 *c*) into essentially three domains: (*a*) a large domain on one end of the molecule of dimensions 54 Å × 47 Å × 70 Å, which accounts for ~60% of the total molecular volume; (*b*) a smaller central domain that is 54 Å × 24 Å × 60 Å and con-

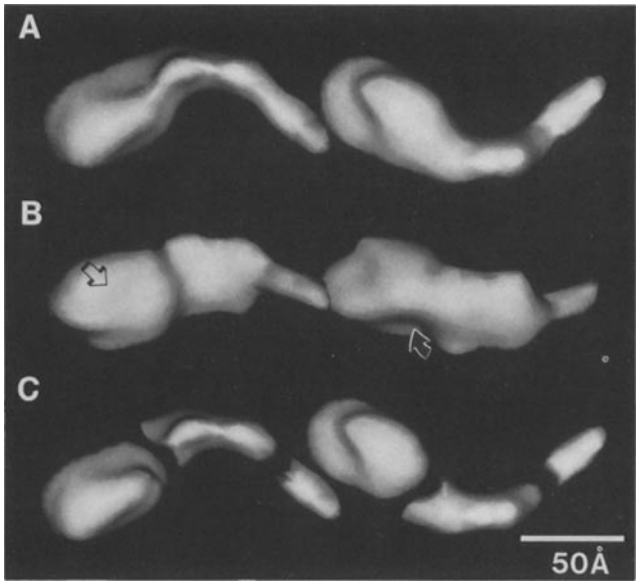

Figure 6. Molecular envelope of myosin S1 produced by averaging two non-crystallographically related molecules about a local two-fold symmetry operator. (*A*) Shaded surface display of two S1 molecules related by a 2_1 screw symmetry operator as in Fig. 5 *B*, but with contacts between the molecules removed. (*B*) The pair of molecules in *A* rotated 60° to reveal the features which subdivide the structure into domains. The curved arrow marks the location of the ATPase site which has been mapped on acto-S1 (Tokunaga et al., 1987*a*), and the straight arrow marks the actin binding surface of myosin S1. (*C*) A pair of molecules as in *A*, which have been separated at domain boundaries.

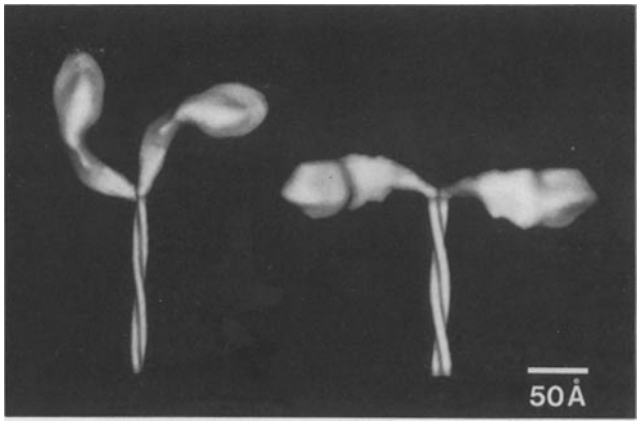

Figure 7. Model of myosin illustrating the arrangement of two S1 molecules about a hypothetical site of rod attachment. A short segment (~160 Å) of myosin rod was modeled based on a coiled-coil α-helix with 162 Å pitch. A pair of S1 molecules are arranged about the rod to produce curved and straight profiles of the myosin heads similar in appearance to myosin observed by electron microscopy. These different profiles can be modeled with the curved S1 structure by rotation about the head–rod junction. Since myosin S1 is produced by proteolysis of the myosin head–rod junction, details of the structure of this junction are unknown and the hypothetical junction is presented here only for illustration of the relationship of the S1 structure to myosin.

stitutes ~30% of the total molecular volume and is separated from the larger domain by a cleft on one side of the molecule; and (*c*) the smallest domain corresponding to a thin, tail-like region with dimensions 22 Å × 22 Å × 40 Å and containing ~10% of the total volume. This tadpole-shaped molecular envelope is very similar in appearance to the pear-shaped myosin heads observed by electron microscopy of rotary shadowed and negatively stained myosin and myosin S1 (Flicker et al., 1983; Walker et al. 1985; Winkelmann and Lowey, 1986; Walker and Trinick, 1988, 1989; Vibert, 1988).

Models of Myosin and Acto-S1

The relationship of the structure of S1 to the heads of myosin is illustrated in Fig. 7, in which two S1 molecules have been oriented on the end of a short segment of the myosin rod. The structure of myosin S1 which we have determined provides no details of the head–rod junction; thus, this model is presented primarily to illustrate our interpretation of the results. Two different profiles are presented: a tapered and curved profile of the heads and a straight profile; both of these very different profiles can be generated from the curved S1 structure by rotation about the attachment site with the rod. The length of the heads on the modeled myosin molecule (165 Å) are somewhat shorter than the measured lengths of myosin heads (180-200 Å). This may reflect the uncertainty in the details of the head–rod junction in the model.

The interaction of myosin S1 with actin has been extensively studied by helical 3D reconstruction of S1 decorated actin filaments (acto-S1). Milligan and Flicker (1987) have used cryo-electron microscopy of thin filaments and F-actin both decorated with myosin S1 and helical 3D reconstruction to produce highly reproducible maps of this structure and to define the surface binding site on actin for myosin S1 (Milligan et al., 1990). To compare our results to this reconstruction and construct a model of the structure of rigor acto-S1, we began with the structure of the actin filament. At a resolution of ~20 Å the actin monomer can be represented as a two domain structure and a model of the actin filament based on image analysis of single filaments has been proposed (Egelman and DeRosier, 1983). We started with this model of actin and docked the S1 structure on the actin monomer to generate a model structure for acto-S1. We systematically varied the orientation of the myosin S1 on the actin monomer using the geometry defined by the helical reconstruction of actin-S1 complexes reported by Milligan and Flicker (1987). The quality of the fit of the resulting models to the helical reconstructions of acto-S1 was evaluated by comparing views of the model to reconstructed acto-S1 and by comparing the calculated Fourier transform of the modeled structures to the observed acto-S1 transform.

We have obtained a good fit of the modeled acto-S1 complex to the observed density distributions of negatively stained and frozen-hydrated acto-S1 (Fig. 8). This was evaluated quantitatively for the first, fourth, fifth, sixth, and seventh layer line data and qualitatively for the equator, second and third layer lines (data not shown). In the model, the largest S1 domain primarily attaches to the outer domain of a single actin monomer with the long axis of the actin monomer lying almost parallel in projection to the long axis of the large domain. The distribution of mass in the large domain of S1 is very similar to distribution of mass in the acto-S1 reconstruction. The greatest variation between this model

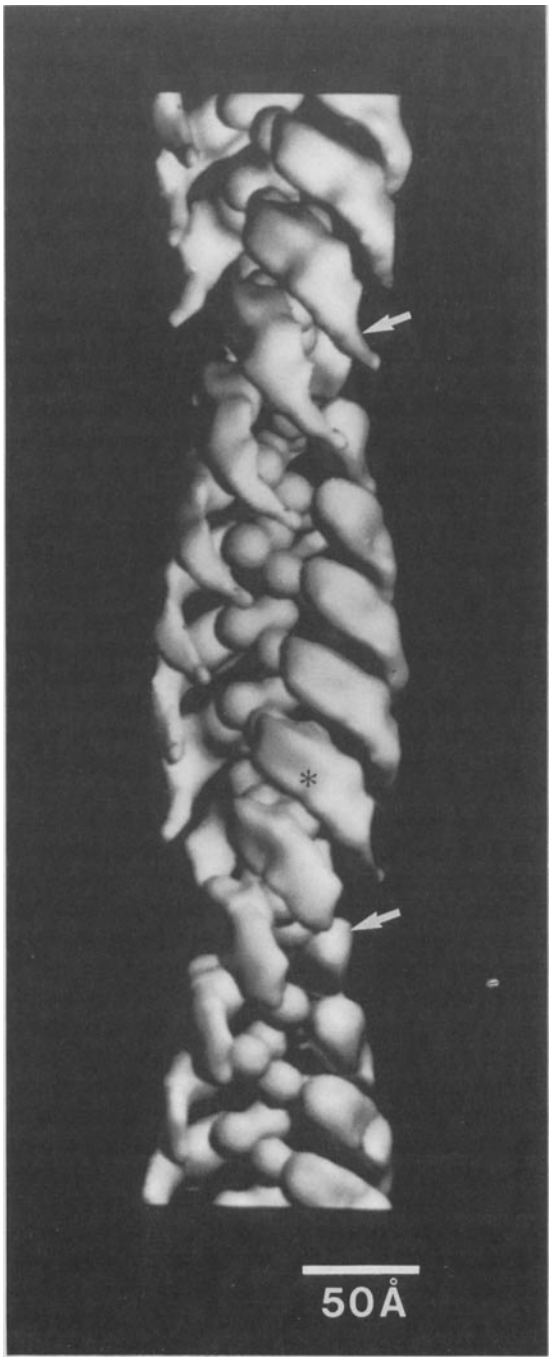

Figure 8. Model of myosin S1 rigor complex with F-actin. The shaded surface model was created by orienting the molecular envelope of myosin S1 on a model of an actin monomer using the geometry for this complex defined by the helical reconstruction of acto-S1 reported by Milligan and Flicker (1987). The model spans two crossovers (760 Å) of the long-pitch actin helix. In the figure, the upper arrow points at the small tail-like domain of myosin S1 that is not generally detected in helical reconstructions of acto-S1. The lower arrow points at one of a group of S1 molecules from which this domain was omitted. Acto-S1 models built lacking this feature of S1 more accurately fit the observed structure of acto-S1. The asterisk highlights the location of the ATPase site mapped on acto-S1 by Tokunaga et al., 1987*a*. This site corresponds to a cleft and indentation in the structure of myosin S1 that was used to subdivide the molecule into the large and central domains.

and helical reconstructions is found in the lower density portions of the structure at higher radius: the central and the smallest domains of myosin S1. The small domain is completely missing in reconstructions of acto-S1 and removal of this region from S1 results in a model of acto-S1 that is most similar to the structure determined by helical reconstruction.

The structure of the actin monomer has been solved at atomic resolution (Kabsch et al., 1990), and an atomic model of the actin filament has been constructed and features of this model have been confirmed by cryoelectron microscopy (Milligan et al., 1990). The structure of myosin S1 and the model for the association between actin and myosin provide a starting point for defining the contact sites between these proteins.

Discussion

Reliability of the S1 Reconstruction

Reconstruction of the 3D density from thin-sectioned crystals of myosin S1 by the systematic approach outlined here has produced a reliable model of the structure of the myosin head at a resolution of ~25 Å. The interpretation of the density distribution in the map and the molecular envelope of myosin S1 is of course dependent on the mechanism of stain penetration and contrast enhancement in the tannic acid–embedded crystals. In the analysis of the packing of S1 in the crystal lattice by both x-ray diffraction of native hydrated crystals and electron microscopy of tannic acid fixed, embedded and sectioned crystals, we found the stain distribution in the fixed and embedded crystals is closely related to the location of solvent regions in native, hydrated crystals (Winkelmann et al., 1985). The contrast in the sections is thus similar to a negatively stained specimen with the regions containing protein surrounded by electron dense stain precipitates. In addition to providing contrast, the stain precipitates impart considerable stability to the crystal section; we observed <10% shrinkage of the lattice dimensions in the direction normal to the electron beam as a consequence of irradiation during image collection.

Structural Details of Myosin S1 Crystal Lattice

The interpretation of the stain excluding molecular envelope of myosin S1 revealed in the final symmetry-averaged map is supported by the results of the analysis of the packing of S1 in the crystal lattice (Winkelmann et al., 1985). There are eight S1 molecules in the unit cell with two in each asymmetric unit. The molecules are arranged in layers that nearly superimpose except for a translation of ~9 Å along the *c* axis. Given the unit cell dimensions, the eight molecules of S1 occupy 36% of the unit cell. Interpretation of the map using this volume as a cut-off for determining the boundary between protein and solvent reveals the elongated, tadpole-shaped stain excluding region previously interpreted as corresponding to a single myosin head in projection (Winkelmann et al., 1985). Changing this cut-off value up or down by 20–30% had little effect on the overall shape of the envelope, but did increase or decrease the contacts between molecules within a layer and between the layers. The envelope of a single molecule was defined by setting the contour level at a value that includes 30% of the unit cell volume (83% of S1 volume).

At this level the S1 molecule has the elongated and curved projection characteristic of rotary-shadowed electron micrographs of this subfragment (Winkelmann and Lowey, 1986).

Shape and Domain Structure of Myosin S1

The S1 structure can be divided into three morphological domains. The largest domain is on one end of the molecule and corresponds to ~60% of the total molecular volume. It is separated from the central domain by a shallow cleft on one side of the molecule, and the long axis of the central domain is bent away from the long axis of the large domain. The central domain contains ~30% of the volume of S1, and is distinguished from the smallest domain by an abrupt change in thickness. The smallest domain participates in what appears to be important contacts in the packing of the heads within a layer, and these probably help to hold the crystal lattice together.

Considerable evidence suggests that there are domains in the myosin head that fall near the boundaries described here (reviewed by Vibert and Cohen, 1988). Electron microscopy of negatively stained myosin reveals clefts that can be penetrated by stain and that divide the head into one large and one or two smaller domains (Walker and Trinick, 1988). The size of the largest feature is quite similar to the size and volume of the large distal domain described here. Single particle averaging of shadowed myosin also reveals a multidomain structure: a large domain separated by a cleft from a slimmer, more variable region of the head near the head–rod junction (Vibert, 1988). The narrow region appears to adopt a variety of configurations and this apparent flexibility or distortion limited the detail that was seen in this part of the averaged structure.

The 25-kD amino-terminal proteolytic fragment of myosin S1 contains sequences implicated in ATP binding (Walker et al., 1982); in addition, photoreactive analogues of ATP label-specific residues in this fragment and in the 50-kD central fragment, suggesting that sequences from both of these proteolytic fragments are involved in ATP binding (Mahmood and Yount, 1984; Okamoto and Yount, 1985). Residues in the 50-kD fragment and near the 50-kD–20-kD junction have been cross-linked to actin (Mornet et al., 1981*a*; Sutoh, 1983), suggesting that portions of the 50-kD fragment may interact with actin. Epitopes in the 25- and 50-kD fragments and the nucleotide binding site have been located on the distal portion of the head (Winkelmann and Lowey, 1986; Sutoh et al., 1986). These results place at least part of the 25- and 50-kD fragments in the large domain of S1. These fragments account for 58% of the mass of myosin S1 and, thus, are comparable in size to the large domain of the molecular envelope.

The 20-kD fragment contains the reactive sulfhydryls SH_1 and SH_2. These are on cysteine residues separated by only 10 amino acids in a mobile segment of the heavy chain. The SH_1 cystine has been localized ~130 Å from the head–rod junction (Sutoh et al., 1984). The 20-kD fragment also contains sites involved in light chain binding to the heavy chain. Sites near the amino and carboxy termini of both myosin light chains have been mapped by immunoelectron microscopy to the narrow region of the head within 100 Å of the head–rod junction (Flicker et al., 1983; Winkelmann and Lowey, 1986; Tokunaga, et al., 1987*b*; Katoh and Lowey, 1989), and a discrete proteolytic fragment of myosin that contains the 20-kD fragment with the associated light chains has been visualized by electron microscopy and appears to comprise most of the mass of the narrow region of the head (Winkelmann et al., 1984). These data suggest that the elongated 20-kD fragment with bound light chains corresponds to the combined central and small tail-like domains of the S1 structure.

Modeling Myosin and Acto-S1

The relationship of the S1 structure to myosin and acto-S1 is summarized in two models (Figs. 7 and 8). The shape and curvature of the heads and overall appearance of the modeled myosin molecule (Fig. 7) is strikingly similar to electron micrographs of myosin contrasted by rotary shadowing or negative staining. The length of the heads on the myosin model are smaller by 15–25 Å than the measured length from electron microscopy of rotary-shadowed and negatively stained myosin molecules. Myosin S1 is prepared by cleavage of the head–rod junction, so details of the structure of this region are not revealed in the reconstruction and cannot be modeled with any reliability, thus, the shorter length of the model myosin heads may reflect uncertainty in the details of the junction. This uncertainty is compounded by recent data that suggests 53 residues of the rod sequence may extend into the myosin head, and proteolytic separation of the heads from the rod may occur at a site within the head (Rimm et al., 1989). Alternatively, the measured length of the head may be exaggerated due to flattening as has been suggested for the measured diameter (Elliott and Offer, 1978; Walker and Trinick, 1988; Vibert, 1988).

The curved and straight head profiles often seen on myosin have been modeled by rotation of the curved S1 structure about the head–rod junction. Several lines of evidence indicate that the heads can rotate freely and independently about the head–rod junction (Craig et al., 1980; Winkelmann and Lowey, 1986; Reedy et al., 1989). In addition to rotation, myosin heads exhibit considerable heterogeneity in the orientation about the head–rod junction and in the degree and direction of curvature within a head (Elliott and Offer, 1978; Craig et al., 1980; Knight and Trinick, 1984; Walker and Trinick, 1988). This may reflect a flexibility in the structure or may result from distortion imposed by surface interactions.

The acto-S1 model (Fig. 8) has the major features identified in all reconstructions of S1 decorated actin filaments: the large S1 domain makes extensive contact with the actin filament, and the attached S1 displays left-handed slew curvature. The geometry of the actin-S1 interface observed in the reconstruction of frozen-hydrated samples of acto-S1 complexes (Milligan and Flicker, 1987) was used for constructing the model. In the acto-S1 reconstruction, S1 is divided into two domains or regions: a high density domain 95 Å long and 45–55 Å in diameter, and a low density domain at higher radius that is 35 Å long and smeared azimuthally. This suggests that the two domains exhibit different degrees of order that may result from intramolecular motion or flexibility. The features of their maps are apparent in the modeled acto-S1 structure. The model differs from the acto-S1 reconstruction only in the radial extent of the central and small tail-like domains, features which are likely to be poorly preserved in helical reconstructions.

Tokunaga et al. (1987*a*) have determined the position of the ATPase site of myosin S1 by computing a 3D reconstruction of acto-S1 with an analogue of ADP covalently bound in the active site. The ATPase site in ~50 Å from the tip of the head and 40 Å away from and opposite the actin binding interface of S1. Our model of the acto-S1 agrees very well with this reconstruction. The location of the ATPase site corresponds to the indentation or cleft observed in the S1 structure at the boundary between the large and central domains (Fig. 8).

The thin tail-like domain of S1, which is missing from 3D reconstructions of acto-S1, can be seen in the 3D reconstruction of insect indirect flight muscle (Taylor et al., 1989*a*,*b*). In this reconstruction, myosin cross-bridges emerge from the thick filament surface as narrow stems that broaden and bend as they approach and form rigor contacts with the thin filaments. The rigor cross-bridges occur in at least two forms: the large lead cross-bridges which consist of a pair of myosin heads, and the smaller rear cross-bridges comprising a single myosin head. The conformational differences between the heads in the lead and rear bridges include variations in bending as well as tilt angle. It is likely that the interface between actin and myosin is the same for all rigor heads, and that combinations of actin filament untwisting and multiple head conformations accommodate the distortion arising from the single actin filament binding of two-headed and one-headed crossbridges. This implies that different conformations of myosin heads exist even in strongly bound states. These results support the view that multiple, flexibly connected domains must be present in the myosin head.

Domain Structure and Models of Muscle Contraction

Biochemical binding studies suggest that myosin S1 exists in at least two conformations (Eisenberg and Hill, 1985). In one conformation, which occurs in the absence of ATP, S1 binds very strongly to actin and detaches from it slowly. In a second conformation, which is induced by ATP binding, S1 binds very weakly to actin and detaches rapidly. It has been proposed that, during a crossbridge cycle, the transition from the weak binding to strong binding conformation causes the elastic myosin crossbridge to become deformed and exert positive force, while the reverse transition (from strong binding to weak binding) causes a deformation that leads to detachment of the crossbridge from actin (Eisenberg and Greene, 1980). Whereas structural evidence for the conformation of the crossbridge in the strong binding state (rigor) is available from x-ray diffraction of rigor muscle and image analysis of rigor complexes of acto-S1 and rigor insect flight muscle, the presence of the weak binding state has only been inferred and little is known about its conformation.

Biochemical and biophysical evidence for intramolecular motion in myosin is available. For example, nucleotide binding to the myosin head causes internal motion that is reflected by changes in the pattern of cross-links that can be formed with SH_1 and by changes in proteolytic susceptibility of bonds (Lu et al., 1986; Applegate and Reisler, 1984). Weak and strong binding states of actin also suggest nucleotide induced motion that dramatically alters actin binding affinity (Eisenberg and Greene, 1980). NMR and electric birefringence studies have demonstrated flexibility in isolated heads (Prince et al., 1981; Highsmith and Eden, 1986). In addition, x-ray diffraction of active heads indicates the existence of internal flexibility and motion (Huxley et al., 1982). In contrast, optical and paramagnetic probes indicate that some regions of the head, especially SH_1 and the ATP binding site, maintain a constant orientation with respect to actin during active contraction (Yanagida, 1981, 1985).

The model described by Huxley and Kress (1985) resolves these apparently contradictory observations by proposing interdomain mobility that occurs during activity and accounts for motion. In this model, muscle cross-bridges can interact with the thin filament over an axial range of 120 Å as originally proposed for the power stroke (Huxley and Simmons, 1971), but the crossbridges produce force with a more limited axial movement of 40 Å. This magnitude of change could be accommodated by movement within a part of the S1 structure or between domains within the structure leaving a portion of the structure in a static configuration with respect to actin. This model satisfies the experimental observations which indicate a fixed orientation of labeled probes located in the active site and on SH_1 during isometric contraction, if the labeled probes are located on a portion of the structure which does not move. In terms of the structure presented here, the large domain is the likely location of these sites and, thus, would maintain a fixed orientation with respect to actin. The mobile elements of the crossbridge would then be the central and small domains, and movement would be the result of interdomain flexibility, e.g., at junctions between domains. Solution of the high-resolution crystal structure of myosin S1 will further delineate domain boundaries and provide more definitive information concerning the possibility of such interdomain flexibility.

We thank G. Sosinsky and D. L. D. Caspar for advice and for sharing their ideas about the reliability index, H. MeKeel for microtomy and P. Somu for help with programming.

This work is supported by grants from the Muscular Dystrophy Association and the National Institutes of Health (NIH) (AR38454) to D. A. Winkelmann, Established Investigator awards from the American Heart Association to D. A. Winkelmann and to I. Rayment, and by NIH grant GM33050 to T. S. Baker and NIH grant AR35186 to I. Rayment.

Received for publication 4 March 1991 and in revised form 3 May 1991.

References

Agard, D. A. 1983. A least-squares method for determining structure factors in three-dimensional tilted-view reconstructions. *J. Mol. Biol.* 167:849–853.

Agard, D. A., and R. M. Stroud. 1982. Linking regions between helices in bacteriorhodopsin revealed. *Biophys. J.* 37:589–602.

Akey, C. W., K. Moffat, D. C. Wharton, and S. J. Edelstein. 1980. Characterization of crystals of a cytochrome oxidase (nitrate reductase) from *Pseudomonas aeruginosa* by electron diffraction and electron microscopy. *J. Mol. Biol.* 136:19–43.

Amos, L. A., R. Henderson, and P. N. T. Unwin. 1982. Three-dimensional structure determination by electron microscopy of two-dimensional crystals. *Prog. Biophys. Mol. Biol.* 39:183–231.

Applegate, D., and E. Reisler. 1983. Protease-sensitive regions in myosin subfragment 1. *Proc. Natl. Acad. Sci. USA.* 80:7109–7112.

Applegate, D., and E. Reisler. 1984. Nucleotide-induced changes in the proteolytically sensitive regions of myosin subfragment 1. *Biochemistry.* 23:4779–4784.

Baker, T. S. 1981. Image processing of biological specimens: a bibliography. *In* Electron Microscopy in Biology. J. D. Griffith, editor. Wiley-Interscience, New York. 189–290.

Baker, T. S., and L. A. Amos. 1978. Structure of the tubulin dimer in zinc-induced sheets. *J. Mol. Biol.* 123:89–106.

Baker, T. S., D. L. D. Casper, C. J. Hollingshead, and D. A. Goodenough. 1983. Gap junction structures. IV. Asymmetric features revealed by low-irradiation microscopy. *J. Cell Biol.* 96:204–216.

Balint, M., I. Wolf, A. Tarcsafalvi, J. Gergeley, and F. Sreter. 1978. Location of SH-1 and SH-2 in the heavy chain segment of heavy meromyosin. *Arch. Biochem. Biophys.* 190:793–799.

Berger, J. E. 1969. Optical diffraction studies of crystalline structures in electron micrographs. *J. Cell Biol.* 43:442–447.

Craig, R., A. G. Szent-Gyorgyi, L. Beese, P. Flicker, P. Vibert, and C. Cohen. 1980. Electron microscopy of thin filaments decorated with a Ca^{2+}-regulated myosin. *J. Mol. Biol.* 140:35–55.

DeRosier, D. J., and P. B. Moore. 1970. Reconstruction of three-dimensional images from electron micrographs of structures with helical symmetry. *J. Mol. Biol.* 52:355–369.

Egelman, E. H., and D. J. DeRosier. 1983. A model of F-actin derived from image analysis of isolated filaments. *J. Mol. Biol.* 166:623–629.

Eisenberg, E., and L. Greene. 1980. The relation of muscle biochemistry to muscle physiology. *Annu. Rev. Physiol.* 42:293–309.

Eisenberg, E., and T. L. Hill. 1985. Muscle contraction and free energy transduction in biological system. *Science (Wash. DC).* 227:999–1006.

Elliott, A., and G. Offer. 1978. Shape and flexibility of the myosin molecule. *J. Mol. Biol.* 123:505–519.

Erickson, H. P., and A. Klug. 1971. Measurement and compensation of defocusing and aberrations by Fourier processing of electron micrographs. *Phil. Trans. R. Soc. Lond. B. Biol.* 261:105–118.

Flicker, P. F., T. Wallimann, and P. Vibert. 1983. Electron microscopy of scallop myosin: location of the regulatory light chains. *J. Mol. Biol.* 169:723–741.

Highsmith, S., and D. Eden. 1986. Myosin subfragment 1 has tertiary structural domains. *Biochemistry.* 25:2237–2242.

Huxley, A. F., and R. M. Simmons. 1971. Proposed mechanism of force generation in striated muscle. *Nature (Lond.).* 233:533–538.

Huxley, H. E., and M. Kress. 1985. Crossbridge behaviour during muscle contraction. *J. Muscle Res. Cell Motil.* 6:153–161.

Huxley, H. E., A. R. Faruqi, M. Kress, J. Bordas, and M. H. J. Koch. 1982. Time resolved X-ray diffraction studies of the myosin layer-line reflections during muscle contraction. *J. Mol. Biol.* 158:637–684.

Kabsch, W., H. G. Mannherz, S. Suck, E. F. Pai, and K. C. Holmes. 1990. Atomic structure of actin: DNase I complex. *Nature (Lond.).* 347:37–44.

Katoh, T., and S. Lowey. 1989. Mapping myosin light chains by immunoelectron microscopy. Use of anti-fluorescyl antibodies as structural probes. *J. Cell Biol.* 109:1549–1560.

Knight, P., and J. Trinick. 1984. Structure of the myosin projections on native thick filaments from vertebrate skeletal muscle. *J. Mol. Biol.* 177:461–482.

Lowey, S., H. S. Slayter, A. G. Weeds, and H. Baker. 1969. Substructure of the myosin molecule: I. Subfragments of myosin by enzymatic degradation. *J. Mol. Biol.* 42:1–29.

Lu, R. C., L. Moo, and A. G. Wong. 1986. Both the 25-kDa and 50-kDa domains in myosin subfragment 1 are close to the reactive thiols. *Proc. Natl. Acad. Sci. USA.* 83:6392–6396.

Mahmood, R., and R. G. Yount. 1984. Photochemical probes of the active site of myosin. *J. Biol. Chem.* 259:12856–12959.

Margossian, S. S., and S. Lowey. 1973. Substructure of the myosin molecule. IV. Interaction of myosin and its subfragments with adenosine triphosphate and F-actin. *J. Mol. Biol.* 74:313–330.

Margossian, S. S., W. F. Stafford III, and S. Lowey. 1981. Homogeneity of myosin subfragments by equilibrium centrifugation. *Biochemistry.* 20:2151–2155.

Milligan, R. A., and P. F. Flicker. 1987. Structural relationships of actin, myosin and tropomyosin revealed by cryo-electron microscopy. *J. Cell Biol.* 105:29–39.

Milligan, R. A., M. Whittaker, and D. Safer. 1990. Molecular structure of F-actin and location of surface binding sites. *Nature (Lond.).* 348:217–221.

Mornet, D., R. Bertrand, P. Pantel, E. Audemard, and R. Kasab. 1981*a*. Structure of the actin-myosin interface. *Nature (Lond.).* 292:301–306.

Mornet, D., R. Bertrand, P. Pantel, E. Audemard, and R. Kasab. 1981*b*. Proteolytic approach to structure and function of actin recognition sites in myosin heads. *Biochemistry.* 20:2110–2119.

Okamoto, Y., and R. G. Yount. 1985. Identification of an active site peptide of skeletal myosin after photoaffinity labeling with N-(4-azido-2-nitrophenyl)-2-aminoethyl diphosphate. *Proc. Natl. Acad. Sci. USA.* 82:1575–1579.

Pollard, T. D., S. K. Doberstein, and H. G. Zot. 1991. Myosin-I. *Annu. Rev. Physiol.* 53:653–681.

Prince, H. P., H. R. Trayer, G. D. Henry, I. P. Trayer, D. C. Dalgarno, B. A. Levine, P. D. Cary, and C. Turner. 1981. Proton nuclear magnetic resonance spectroscopy of myosin subfragment 1 isoenzymes. *Eur. J. Biochem.* 121:213–219.

Rayment, I., and D. A. Winkelmann. 1984. Crystallization of myosin subfragment-1. *Proc. Natl. Acad. Sci. USA.* 81:4378–4380.

Reedy, M. C., C. Beall, and E. Fyrberg. 1989. Formation of reverse rigor chevrons by myosin heads. *Nature (Lond.).* 339:481–483.

Rimm, D. L., J. H. Sinard, and T. D. Pollard. 1989. Location of the head-tail junction of myosin. *J. Cell Biol.* 108:1783–1789.

Salmon, E. D., and D. DeRosier. 1981. A surveying optical diffractometer. *J. Microsc.* 123:239–247.

Shaw, P. J., and G. J. Hills. 1981. Tilted specimen in the electron microscope: a simple specimen holder and the calculation of tilt angles for crystalline specimens. *Micron.* 12:279–282.

Sutoh, K. 1983. Mapping of actin-binding sites on the heavy chain of myosin subfragment 1. *Biochemistry.* 22:1579–1585.

Sutoh, K., K. Yamamoto, and T. Wakabayashi. 1984. Electron microscopic visualization of the SH_1 thiol of myosin by the use of an avidin-biotin system. *J. Mol. Biol.* 178:323–339.

Sutoh, K., K. Yamamoto, and T. Wakabayashi. 1986. Electron microscopic visualization of the ATPase site of myosin by photoaffinity labeling with a biotinylated photoreactive ADP analog. *Proc. Natl. Acad. Sci. USA.* 83:212–216.

Taylor, K. A., M. C. Reedy, L. Cordova, and M. K. Reedy. 1989*a*. Three-dimensional image reconstruction of insect flight muscle. I. The rigor myac layer. *J. Cell Biol.* 109:1085–1102.

Taylor, K. A., M. C. Reedy, L. Cordova, and M. K. Reedy. 1989*b*. Three-dimensional image reconstruction of insect flight muscle. II. The rigor actin layer. *J. Cell Biol.* 109:1103–1123.

Tokunaga, M., K. Sutoh, C. Toyoshima, and T. Wakabayashi. 1987*a*. Location of the ATPase site of myosin determined by three-dimensional electron microscopy. *Nature (Lond.).* 329:635–638.

Tokunaga, M., M. Suzuki, K. Saeki, and T. Wakabayashi. 1987*b*. Position of the amino terminus of myosin light chain 1 and light chain 2 determined by electron microscopy with monoclonal antibody. *J. Mol. Biol.* 194:245–255.

Toyoshima, Y. Y., S. J. Kron, E. M. McNally, K. R. Niebling, C. Toyoshima, and J. A. Spudich. 1987. Myosin subfragment-1 is sufficient to move actin filaments in vitro. *Nature (Lond.).* 328:536–539.

Vibert, P. J. 1988. Domain structure of the myosin head in correlation-averaged images of shadowed molecules. *J. Muscle Res. Cell Motil.* 9:147–155.

Vibert, P., and C. Cohen. 1988. Domains, motion and regulation in the myosin head. *J. Muscle Res. Cell Motil.* 9:296–305.

Walker, J. E., M. Saraste, M. J. Runswick, and M. J. Gay. 1982. Distantly related sequences in the α- and β-subunits of ATP synthase, myosin, kinases and other ATP-requiring enzymes and a common nucleotide binding fold. *EMBO (Eur. Mol. Biol. Organ.) J.* 1:945–951.

Walker, M., and J. Trinick. 1988. Visualization of domains in native and nucleotide-trapped myosin heads by negative staining. *J. Muscle Res. Cell Motil.* 9:359–366.

Walker, M., and J. Trinick. 1989. Electron microscopy of negatively stained scallop myosin molecules: effect of regulatory light chain removal. *J. Mol. Biol.* 208:469–475.

Walker, M., P. Knight, and J. Trinick. 1985. Negative staining of myosin molecules. *J. Mol. Biol.* 184:535–542.

Warrick, H. M., and J. A. Spudich. 1987. Myosin structure and function in cell motility. *Annu. Rev. Cell Biol.* 3:379–421.

Weeds, A. G., and R. S. Taylor. 1975. Separation of subfragment-1 isoenzymes from rabbit skeletal muscle myosin. *Nature (Lond.).* 257:54–56.

Winkelmann, D. A., and S. Lowey. 1986. Probing myosin head structure with monoclonal antibodies. *J. Mol. Biol.* 188:595–612.

Winkelmann, D. A., S. Alameda, P. J. Vibert, and C. Cohen. 1984. A new myosin fragment: visualization of the regulatory domain. *Nature (Lond.).* 307:758–760.

Winkelmann, D. A., H. Mekeel, and I. Rayment. 1985. Packing analysis of crystalline myosin subfragment-1: implications for the size and shape of the myosin head. *J. Mol. Biol.* 181:487–501.

Yanagida, T. 1981. Angles of nucleotides bound to crossbridges in glycerinated muscle fibers at various concentrations of ϵATP, ϵADP and ϵAMPPNP detected by polarized fluorescence. *J. Mol. Biol.* 146:539–560.

Yanagida, T. 1985. Angles of active site of myosin heads in contracting muscle during sudden length changes. *J. Muscle Res. Cell Motil.* 6:43–52.